FRONTIERS OF PHYSICS

TOPICAL REVIEW
Volume 17 / Issue 4 / 43202 / 2022

Transition metal dichalcogenides (TMDCs) heterostructures: Optoelectric properties

Rui Yang, Jianuo Fan, Mengtao Sun†

School of Mathematics and Physics, Beijing Advanced Innovation Center for Materials Genome Engineering,
University of Science and Technology Beijing, Beijing 100083, China
Corresponding author. E-mail: †mengtaosun@ustb.edu.cn
Received February 1, 2022; accepted May 23, 2022

ABSTRACT

Transition metal dichalcogenides (TMDCs) have suitable and adjustable band gaps, high carrier mobility and yield. Layered TMDCs have attracted great attention due to the structure diversity, stable existence in normal temperature environment and the band gap corresponding to wavelength between infrared and visible region. The ultra-thin, flat, almost defect-free surface, excellent mechanical flexibility and chemical stability provide convenient conditions for the construction of different types of TMDCs heterojunctions. The optoelectric properties of heterojunctions based on TMDCs materials are summarized in this review. Special electronic band structures of TMDCs heterojunctions lead to excellent optoelectric properties. The emitter, p-n diodes, photodetectors and photosensitive devices based on TMDCs heterojunction materials show excellent performance. These devices provide a prototype for the design and development of future high-performance optoelectric devices.

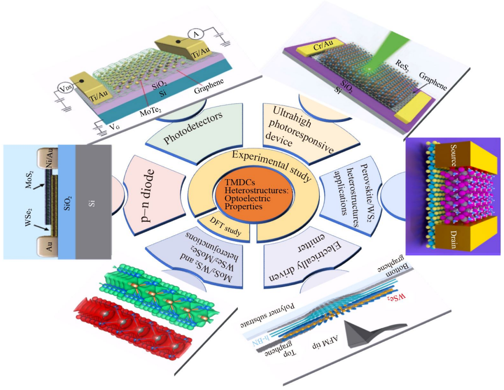

Keywords transition metal dichalcogenides (TMDCs), heterostructures, optoelectric properties

Contents

1 Introduction

Graphene has sparked a wave of research into two-dimensional (2D) materials since its discovery in 2004 [1]. The discovery of graphene has changed the understanding of traditional nanomaterials and opened the door of novel 2D nanomaterials. Subsequently, 2D materials such as black phosphorus [2, 3], transition metal dichalcogenides (TMDCs) [4], borophene [5, 6], and

Higher Education Press

https://doi.org/10.1007/s11467-022-1176-z

others [7] aroused the interest of researchers. The structure formed by the upper and lower layers of chalcogen elements sandwiching a layer of transition metal elements is called transition metal dichalcogenides (TMDCs) [8], whose chemical formula is MX_2, M stands for transition metal element, which is sixfold coordination, and X stands for chalcogen, which is threefold coordination [9]. And some of the structures belong to the lattice structure of the hexagonal system, and some belong to the lattice structure of the triangular system. The TMDCs layers are connected by weak van der Waals force (vdW), while the M and X atoms within the layer are connected by covalent bonds (M-X bonds) [10]. The layered transition metal dichalcogenides, such as $MoSe_2$, MoS_2, WSe_2 and WS_2, are semiconductors and the wavelengths corresponding to the band gaps of TMDCs are between the infrared region and the visible light region [11, 12]. TMDCs show excellent electrical [13, 14], optical [15–18] and catalytic [19] properties. Due to these excellent properties, TMDCs can serve as candidate materials for optoelectronic devices [16, 20], photovoltaic devices [21], energy storage devices [10, 22, 23], catalysis [24], etc.

Van der Waals heterojunctions composed of TDMCs have not only ultrathin, flat, and almost defect-free surfaces, but also excellent mechanical flexibility [25] and chemical stability [26–29]. More importantly, van der Waals heterojunctions combine the excellent properties of two or more constituent materials into one, and can exhibit better electrical, optical [4, 30–32] and catalytic properties [33]. TMDCs materials can form vertical heterojunctions and horizontal heterojunctions. TDMCs heterojunctions provide new physical properties and improved device performance, which can be synthesized by Chemical Vapor Deposition (CVD) [34], dry transfer [35] and epitaxial growth [36] methods. As one of the most competitive materials in the design of optoelectrical devices, TMDCs materials have the advantages of wide detection wavelength range, high photoresponsivity, and sensitivity to polarization. TMDCs heterojunctions can be used in optoelectronic devices [37, 38], particularly in light-emitting diodes (LEDs) [39], fabricating field-effect transistor (FET) [40], p-n diodes [41], etc.

2 Transition metal dichalcogenides (TMDCs) heterostructures

Appropriate band gap of 2D materials is an important parameter for their application in optoelectronic devices. Figure 1 is the band gap of several common 2D materials. Among them, TMDCs materials have attracted the attention of researchers due to their tunable band gaps [42]. The band gap of TMDCs can be adjusted by changing thickness or forming heterojunctions with other materials. The semiconducting TMDCs are mainly the 2H phase [43]. For example, the graphene/MoS_2 heterojunction is a direct bandgap semiconductor with a bandgap of 2 meV at K point [44]. MoS_2/h-BN shows the property of indirect band gap with a CBM at the K point and a VBM at the Γ point and increasing the number of h-BN layers will cause the band gap to decrease [45, 46]. The band gap of $MoTe_2$ is about 1 eV, which can be used as infrared photodetector, but the small mobility of $MoTe_2$ limits its application in optoelectronic devices. The combination of $MoTe_2$ and graphene to form a heterojunction can solve this problem [47]. TMDCs/metal/TMDCs/graphene heterostructure materials can be used to design high-sensitivity angular and phase SPR sensors [48]. TMDCs-based 2D heterostructures can be formed by two types of stacking, horizontal and vertical stacking. The former is usually synthesized by “bottom-up” method, while the latter can be synthesized by “bottom-up” and “top-down” methods [49].

According to the different arrangement characteristics of valence and conduction bands of heterojunction materials at the interface, the heterojunctions can be divided into three types, straddling, staggered and broken heterojunctions as shown in Fig. 2. Each type can be applied to different kinds of equipment. Straddling heterojunctions are widely used in optical devices, such as light-emitting diodes (LEDs) [50], due to electrons and holes can be spatially confined, allowing for effective restructuring. Staggered heterojunctions have the potential to be used as unipolar electronic devices because a higher offset (conduction or valence band) on one side

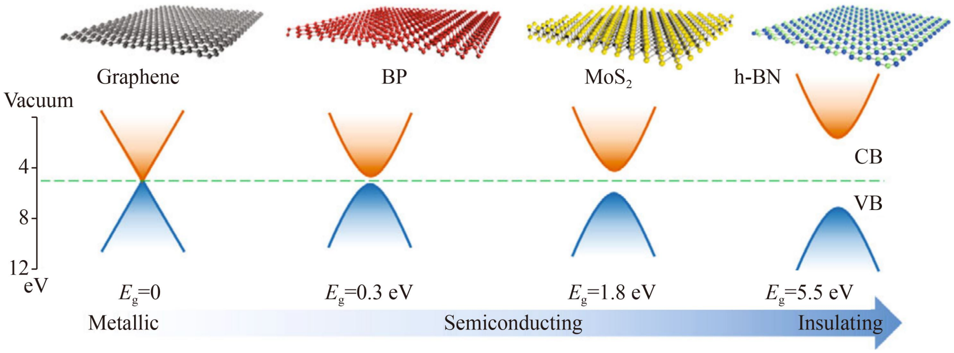

Fig. 1 Structure and energy bands of common two-dimensional materials (Graphene, BP, MoS_2 and h-BN) [51].

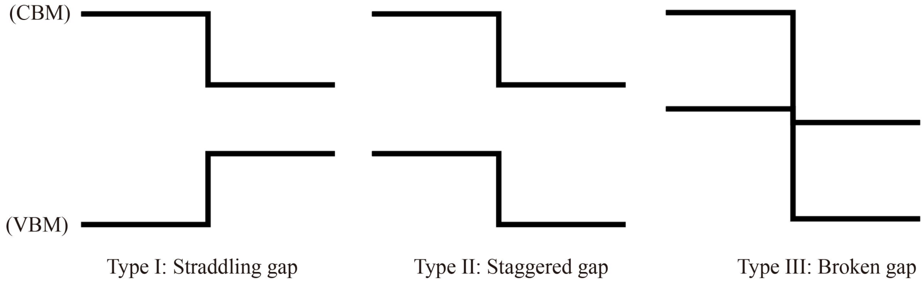

Fig. 2 Energy band characteristics of different types of heterojunctions.

could occur in this type of heterojunction, and results in extremely strong carrier limitations [30]. Staggered and broken heterojunctions are widely used in tunneling field effect transistors (TFETs) [52] and wavelength photodetectors [53]. The layered transition metal dichalcogenides (MoS_2, WS_2, and WSe_2) can form staggered heterojunctions. The VBM and CBM of staggered heterojunction are distributed in different transition metal dichalcogenides materials. The position of the conduction band minimum depends on the material with a narrower bandgap, and the position of valence band maximum is related to the material with a wider bandgap. The staggered heterojunction has important application value in the fields of photovoltaic, photoelectric detection and solar cells. All in all, heterojunctions formed by different transition metal chalcogenides can be used to control the generation, transport and transition properties of free carriers, excitons, phonons and photons at the interface of atomic layers. Therefore, the construction of van der Waals heterojunctions by using transition metal chalcogenides provides a new way to utilize materials, which has played a huge role in the research and development of special optoelectronic functional devices [30].

3 First-principles studies of TMDCs heterojunctions

First-principles calculations also play an important role in the study of TMDCs heterojunctions. For example, the calculations of IVB-VIA group TMDCs show that after absorbing photons, electronic transitions mainly occur between the first, second, and third valence band and the first conduction band. The parallel band effect occurs in monolayer structures means that there is strong optics-matter interaction in these TMDCs materials [54]. Calculations for VIIB-VIA group TMDCs show that the band gap is between 1.70 eV and 2.12 eV. And the positions of the highest occupied state in the valence band and the lowest occupied state in the conduction band are mainly determined by the d electron states of the transition metal atoms [11]. The calculations of the IVB-VIA transition metal trisulfide (MX_3) show that it is suitable for photocatalytic water splitting [55].

Mu *et al.* [56] investigated the interfacial charge transfer in vertical and lateral MoS_2/WS_2 heterojunctions by first-principles calculations. The energy bands of the two structures are shown in Fig. 3(a). The dielectric function of the vertical MoS_2/WS_2 heterojunction shows a strong negative real part near 465 nm, which indicates that there is a plasmon effect and manifested as a strong optics-matter interaction. There is a strong charge transfer (CT) exciton peak at 800 nm corresponding to a direct transition and an indirect transition marked in the band, the electrons are located on MoS_2 and the holes are located on WS_2 as shown in Fig. 3(b). For the lateral heterojunction, the imaginary part of the dielectric constant does not show a negative value, so there is no plasmon properties. And there is a weak absorption peak at 700 nm corresponding to the intralayer CT excitons corresponding to the direct transition of Γ point.

By adjusting the radius of the Ag disk, the surface plasmon resonance (SPR) peak of the Ag disk can matched with the SPR peak and CT exciton peak of the heterojunctions, respectively. When the radius of the Ag disk is 75 nm, it matches the SPR peak of the vdW heterojunction, and a strong coupling occurs between them, which makes the SPR peak shift by 124.75 meV, and Rabi splitting occurs. The SPR peak of Ag disk (the radius is 145 nm) matches the CT exciton peak of the vdW heterojunction, and then they are weakly coupled to produce the Purcell effect as shown in Fig. 4(a). Since there is no SPR peak in the lateral MoS_2/WS_2 heterojunction, the SPR peak of Ag is coupled with the CT exciton peak of the heterojunction. When its radius is 40 nm, the SPR peak of Ag is coupled with the strong absorption peak, and Rabi splitting occurs. When the radius of the Ag disk is 88 nm, the SPR of Ag is weakly coupled with CT excitons, resulting in a 90.4 nm shift of the SPR peak as shown in Fig. 4(b).

Fan *et al.* [57] analyzed pressure-dependent charge-transfer excitons in WSe_2–$MoSe_2$ heterostructures in 2021. As the pressure increases, the conduction band of WSe_2 near the Fermi level gradually decreases, and the valence band of $MoSe_2$ near the Fermi level gradually increases, which results in the characteristics of direct and indirect band gaps varying with pressure, and the trend is different, as shown in Fig. 5(a). The effective mass of electrons and holes also changes with pressure, the effective mass of electrons decreases with the

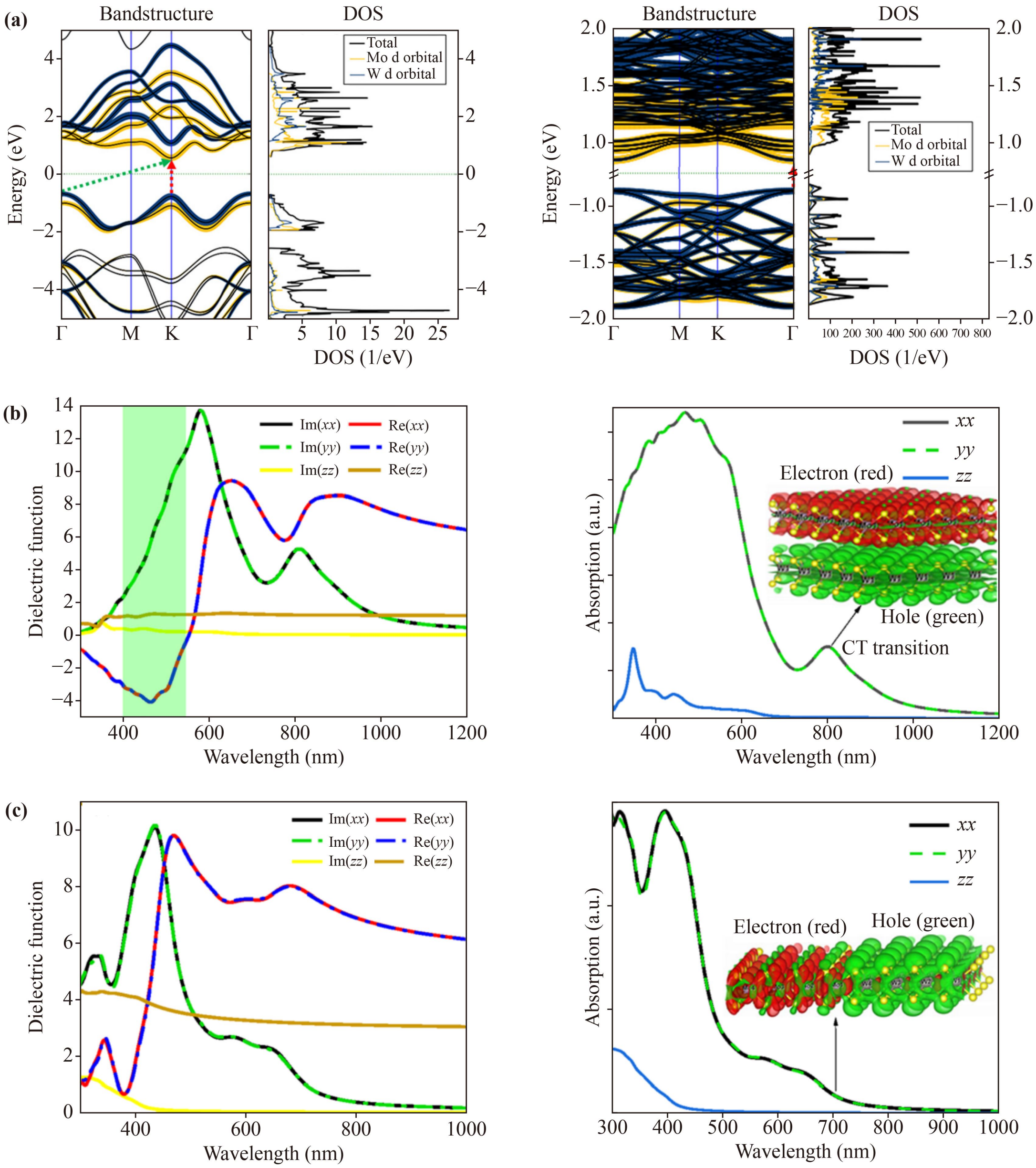

Fig. 3 **(a)** Bands and DOS of vdW and lateral MoS_2/WS_2 heterojunctions. **(b, c)** The dielectric function and absorption of vdW and lateral MoS_2/WS_2 heterojunctions, respectively. Reproduced from Ref. [56].

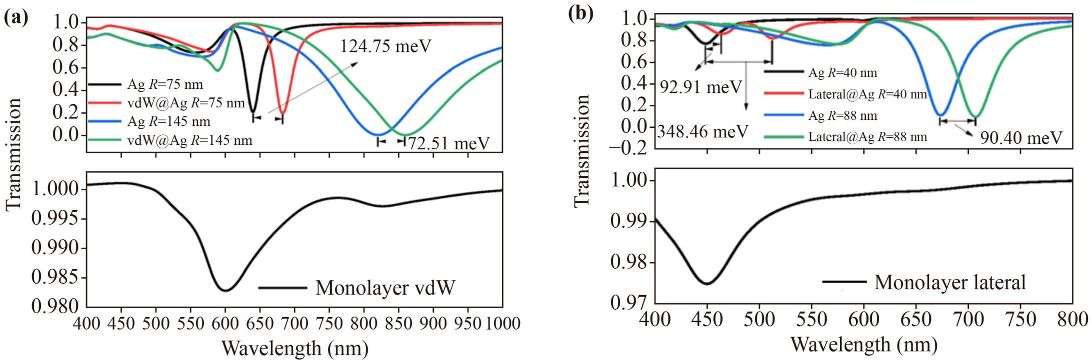

Fig. 4 **(a, b)** Transmission spectra of coupling between Ag disks and vdW and lateral MoS_2/WS_2 heterojunctions, respectively. Reproduced from Ref. [56].

increasing pressure, while that of holes first decreases and then increases [Fig. 5(b)]. The change of energy band and effective mass causes the change of intrinsic carrier concentration. When the pressure increases, the intrinsic carrier concentration of direct band gap first decreases and then increased slightly with a 4.16 GPa pressure, and that of indirect band gap gradually increases as shown in Fig. 5(c). The pressure-dependent absorption spectra show that the CT exciton absorption peak at 825 nm red-shifts with the increasing pressure, which is consistent with the change of energy band. And when the pressure increases to 1.6 GPa, the direction of charge transfer changes. When the pressure continues increasing to 4.16 GPa, the direction of charge transfers no longer changes, but the degree deepens. The increase in pressure reduces the spacing of the heterojunctions and changes the interfacial state of WSe_2–$MoSe_2$ heterojunctions.

4 The optoelectric properties of TMDCs heterostructures

4.1 WSe_2/MoS_2 heterojunction-based p–n diode

The most basic component of most optoelectronic

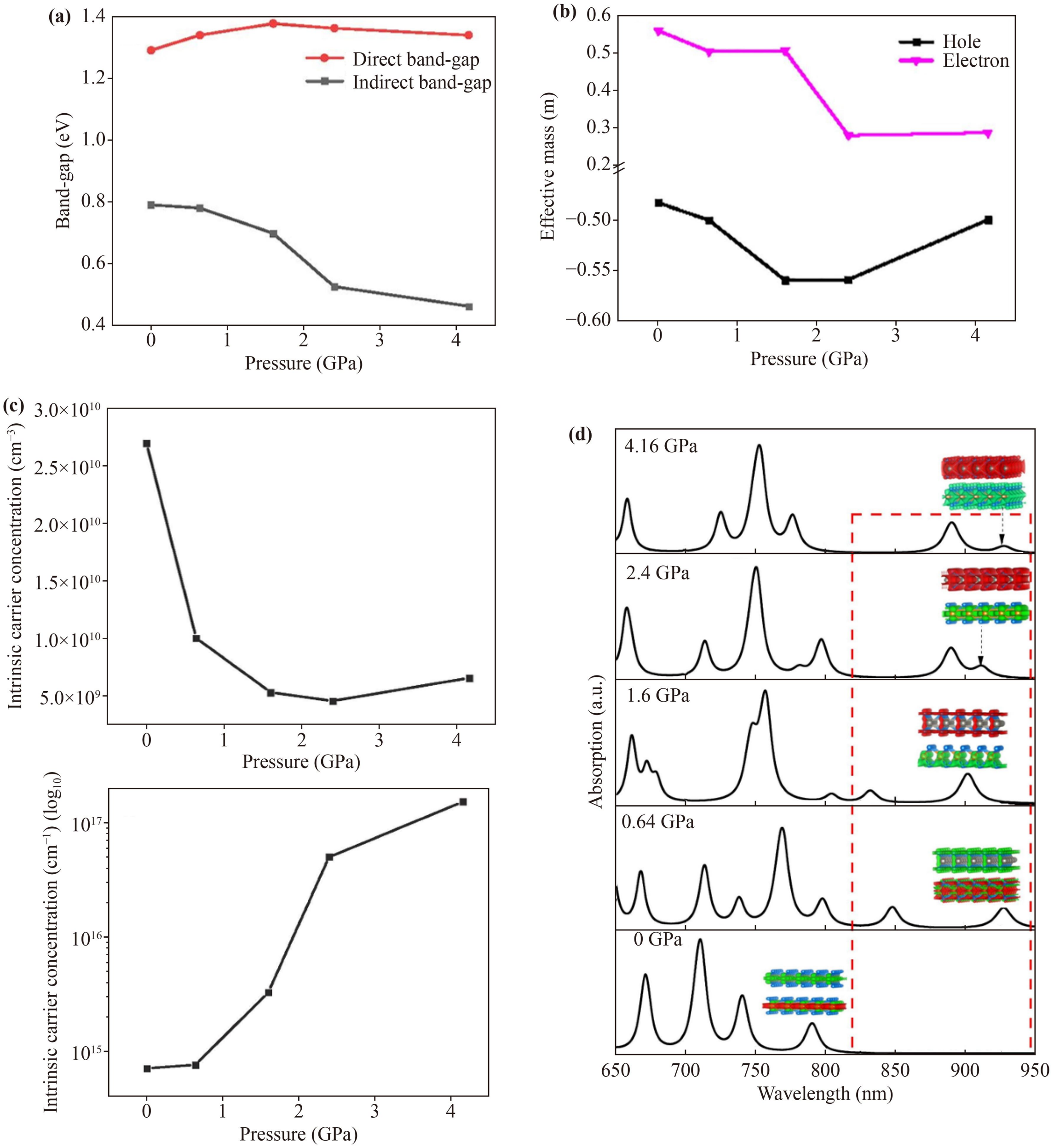

Fig. 5 **(a)** Pressure-dependent direct and indirect band-gap. **(b)** Pressure-dependent effective mass of hole and electron. **(c)** Pressure-dependent intrinsic carrier concentration of indirect and direct band gap. **(d)** Pressure-dependent absorption spectra and the charge distribution. Reproduced from Ref. [57].

devices is the p–n diode [41]. Due to the difficulty in selectively doping TMDCs into p-type or n-type semiconductors, it is very difficult to manufacture p–n diodes in layer TMDCs. Cheng *et al.* [41] synthesized monolayer WSe_2 with 300 nm thick Si/SiO_2 as the substrate, and the triangular region in the center was bilayer [Fig. 6(a)], the exfoliated MoS_2 sheets were transferred to the WSe_2 structure to assemble into a vertical WSe_2–MoS_2 heterojunction [Fig. 6(b)]. Photoluminescence (PL) mapping in Fig. 6(c) can clearly distinguish MoS_2 and WSe_2 layers. The electrodes were established by electron beam lithography and evaporation [Fig. 6(d)].

The PL spectra of the WSe_2 samples exhibit a strong layer-dependent performance [Fig. 7(a)], where the PL intensity of monolayer WSe_2 is 10 times stronger than that of bilayer WSe_2. It can be seen that monolayer WSe_2 shows a PL peak at the wavelength of 785 nm. The PL of bilayer WSe_2 also shows the 785 nm exciton peak and a broad peak at the wavelength of 877 nm, which can be attributed to the indirect band gap emission. There is a peak at 677 nm of the MoS_2 PL spectrum. Figures 7(b) and (c) show a linear relationship between I_{ds} and V_{ds} of MoS_2 and WSe_2, which indicates that both materials achieve Ohmic contacts, so the heterojunction could demonstrate excellent electronic and optoelectronic properties. The current of MoS_2 increases as the positive gate voltage increasing, which is typical n-type semiconductor. On the contrary, the current of the WSe_2 FET increases as the negative gate voltage increasing, and it is the p-type. Once Ohmic contact is formed, the I_{ds}–V_{ds} of the WSe_2/MoS_2 heterojunction shows obvious current rectification behavior. Only when the WSe_2 semiconductor is positively biased, the current can pass through the heterojunction device, suggesting that the formation of a p–n diode in the WSe_2/MoS_2 heterojunction [Fig. 7(d)]. Moreover, due to WSe_2 layer, the current is inversely proportional to the magnitude of the positive V_{g}. If V_{g} is 0, the ideality factor of the heterojunction device is 1.2, and when the gate voltage is −20 V, the ideality factor is 1.3, which indicating that the device shows good diode performance.

The zero-bias photocurrent mapping with 514 nm laser excitation shows that the WSe_2 and MoS_2 overlap region has obvious light response, indicating that p–n junction is formed in the overlap region. Due to the generation of photocurrent depends on the direct bandgap, the ML-WSe_2/MoS_2 area shows larger photocurrent than the BL-WSe_2/MoS_2 region [Fig. 8(a)]. The output characteristic curve of the p—n diode shows that the $V_{\text{open-circuit}}$ is 0.27 V and the $\mathrm{I}_{\text{short-circuit}}$ is 0.22 μA, which indicates obvious photovoltaic effect. And the rapid photo response indicates that it is caused by the generation of photocarrier. Figures 8(c) and (d)

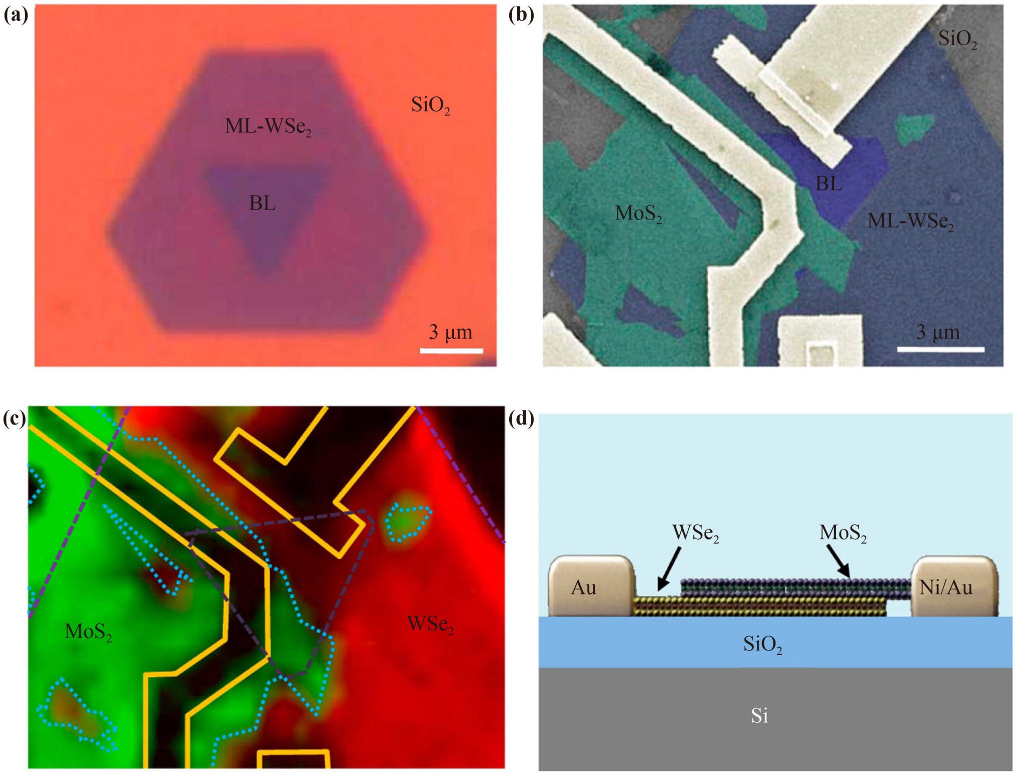

Fig. 6 **(a)** Optical microscopy characterization of the WSe_2. **(b)** The SEM image taken from WSe_2/MoS_2 heterojunction device. **(c)** The PL mapping results of the WSe_2/MoS_2 heterojunction. **(d)** The electrode structure diagram of the WSe_2/MoS_2 heterojunction. Reproduced from Ref. [41].

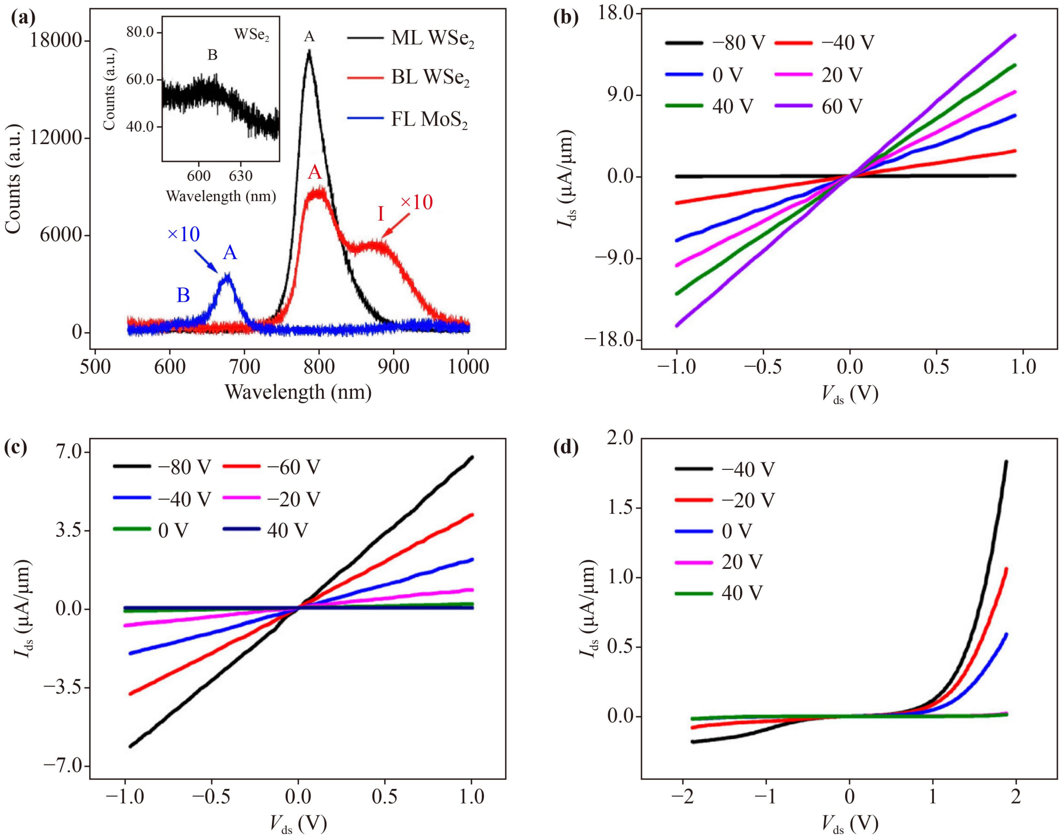

Fig. 7 **(a)** PL spectra of ML WSe_2, BL WSe_2 and FL MoS_2. **(b)** The $I_{ds}-V_{ds}$ curves of MoS_2 FET transistor. **(c)** The $I_{ds}-V_{ds}$ curves of WSe_2 FET transistor. **(d)** Gate-tunable output features of the WSe_2/MoS_2 heterojunction device [41].

show the Electroluminescence (EL) spectra of monolayer WSe_2/MoS_2 heterojunction and bilayer WSe_2/MoS_2 heterojunction, respectively. Their strength increases with the current. Figure 8(e) shows that there are both threshold currents in two types of heterojunctions, and the threshold current of monolayer is lower than that of bilayer heterojunction. Figure 8(f) shows the explanation of the physical mechanism. The potential barrier of hole transport is smaller than that of electron. As the positive bias increases, the holes of WSe_2 transfer to MoS_2, and the electrons cannot overcome the barrier. Because few layers MoS_2 is indirect band gap semiconductor, the yield of radiation composite is relatively low at this time, the EL spectrum is very weak. As V_{bias} increases, the energy of the conduction band minimum of MoS_2 increases, both electrons and holes could overcome the barrier, the radiation composite in WSe_2 is dominant in EL, and the intensity increases linearly with current.

4.2 $MoTe_2$/graphene heterostructure photodetectors

TMDCs materials show excellent performance in photoelectric devices [58], especially in photodetectors [59]. $MoTe_2$ is a special TMDCs material, whose absorption range is located in the near infrared region, which is very suitable for near-infrared photodetectors. The high mobility of graphene [60] can be combined with the high yield of optical carriers in TMDCs materials by forming a heterojunction with graphene [19]. Unlike common TMDCs materials, the band gap of $MoTe_2$ is almost independent of thickness, which is about 1 eV and is suitable for near-infrared Photodetectors. Combined with low resistance and high carrier mobility properties of graphene, multilayer $MoTe_2$, which shows high optical absorption intensity and appropriate band gap, can be assembled into photodetectors with excellent performance. The device can achieve 970.82 $\mathrm{A\cdot W^{-1}}$ photoelectric response at 1064 nm, 4.69×10^8 photoconductive gain and 1.55×10^{11} $\mathrm{Hz^{1/2}\cdot W^{-1}}$ detectivity. Graphene/$MoTe_2$ heterostructure is placed on a Si/SiO_2 substrate, the drain/source electrodes are in contact with graphene, and V_G is connected with Si as shown in Fig. 9(a). The SEM image of photoelectric device is shown in Fig. 9(b). The surface potential profile from graphene to $MoTe_2$ shows that the V_{CPD} of $MoTe_2$ is 58 mV larger than that of graphene. Large difference in work function between probe and material results in large V_{CPD}. Therefore, the work function of $MoTe_2$ is lower than that of graphene, which causes the energy band to tilt towards $MoTe_2$ when the two materials come into contact and create an electric field from $MoTe_2$ to graphene [Fig. 9(d)]. The I_D-V_G characteristic of the heterojunction device was

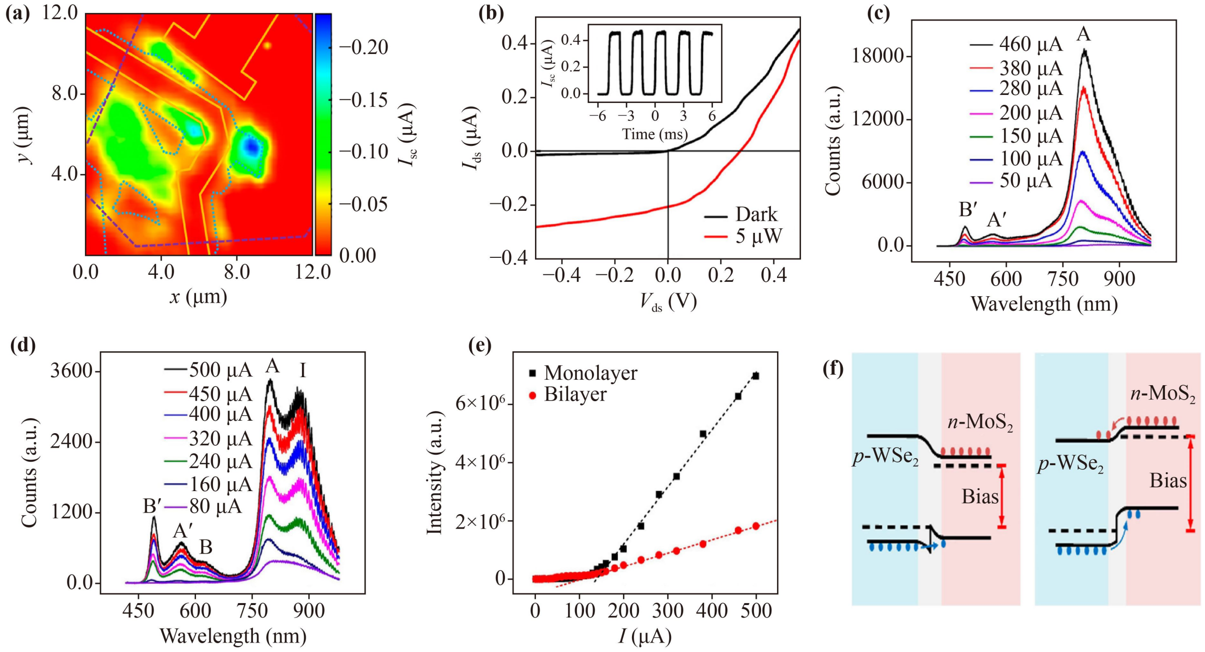

Fig. 8 (**a**) photocurrent intensity map of WSe$_2$/MoS$_2$ heterojunction with 514 nm laser irradiation (V_{ds} and V_{BG} = 0 V). (**b**) $I_{\mathrm{ds}}$$-$$V_{\mathrm{ds}}$ curves of WSe$_2$/MoS$_2$ heterojunction in dark and 514 nm laser irradiation, respectively. (**c**) The EL spectra of ML-WSe$_2$/MoS$_2$ heterojunction with different current. (**d**) The EL spectra of BL-WSe$_2$/MoS$_2$ heterojunction with different current. (**e**) The current-dependent EL strength of ML and BL WSe$_2$/MoS$_2$ heterojunction. (**f**) The explanation of the physical mechanism. Reproduced from Ref. [41].

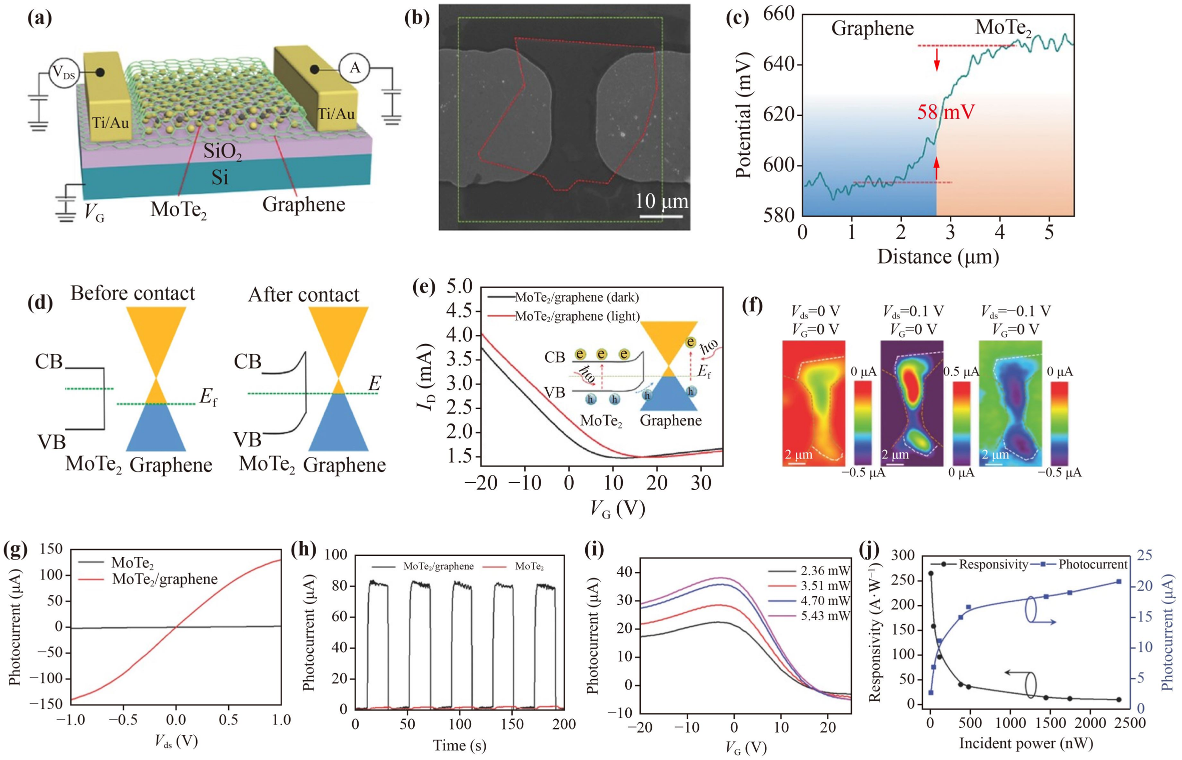

Fig. 9 (**a**) The structure of the MoTe$_2$/graphene phototransistor. (**b**) SEM figure of MoTe$_2$/graphene heterostructure and electrodes. (**c**) The surface potential profile from graphene to MoTe$_2$. (**d**) Band structure of MoTe$_2$ and graphene and their heterojunction. (**e**) Transfer characteristics of the heterostructure in dark and at laser irradiation. (**f**) photocurrent mapping. (**g**) Photocurrents of MoTe$_2$/graphene heterostructure and MoTe$_2$. (**h**) Time-dependent photocurrent of the MoTe$_2$/graphene heterostructure and MoTe$_2$. (**i**) V_{G}-dependent photocurrent with different laser power. (**j**) Relation of photocurrent and photoresponsivity to incident laser power at 980 nm. Reproduced from Ref. [47].

measured with dark and 980 nm illumination, respectively, showing the characteristics of p-type semiconductor. The voltage of charge neutral point in dark condition is smaller than that with light, so there is photogating effect. The scanning photocurrent mapping shows that there is large photocurrent when V_{ds} is 0.1 V. The entire region between the source and drain electrodes shows strong optical response (as shown in Fig. 9(f)) because of the built-in potential. The photocurrent of graphene/$MoTe_2$ heterojunction is 120 times higher than that of $MoTe_2$ at 980 nm incident light and heterojunction shows good repeatability. V_G-dependent photocurrent with different power shows the photocurrent is larger at high power. With a V_G of –3 V, the Fermi level of graphene is located at a suitable location of the photoexcitation hole and it can be effectively transferred from $MoTe_2$ to graphene. When V_G is 16 V, the Fermi level of graphene is located at the Dirac point, with a small slope in the transport and separation of photoexcited carriers, so the photocurrent is very small. Figure 9(j) shows the variation of photocurrent and photo response with incident light power. The photocurrent increases linearly at low power and subsequently saturates due to the increased rate of photoexcited carrier recombination.

4.3 ReS_2/graphene heterostructure ultrahigh photoresponsive device

ReS_2, which exhibits a 1.5 V direct band gap, is a novel TMDCs material. Superimposed TMDCs materials on graphene can improve the response speed and photoresponsivity [47, 61]. In addition, the responsivity of ReS_2 photodetector is 16.14 $A\cdot W^{-1}$, which is very suitable to form heterojunction with graphene as ultra-high photoresponsive device. Figures 10(a) and (b) show the ReS_2/Graphene heterostructure device and the STM image, respectively. Heterojunction exhibits certain metallic properties. Raman spectra clearly show two peaks representing the in-plane and out-of-plane vibration of ReS_2 at 161 cm^{-1} and 217 cm^{-1}, respectively. There is a strong peak at 1.5 eV in PL spectra of both the heterojunction and ReS_2.

When V_G is –30 V, the 550 nm laser with high power can cause the device to produce a larger photocurrent as Fig. 11(a). Responsivity can be expressed by the ratio of photocurrent to laser power [63–65]. Figure 11(b) shows that large laser power corresponds to small responsivity. The calculated responsivity of the heterojunction device is 10^3 times higher than that of ReS_2, which indicates that high carrier transport of graphene greatly improves

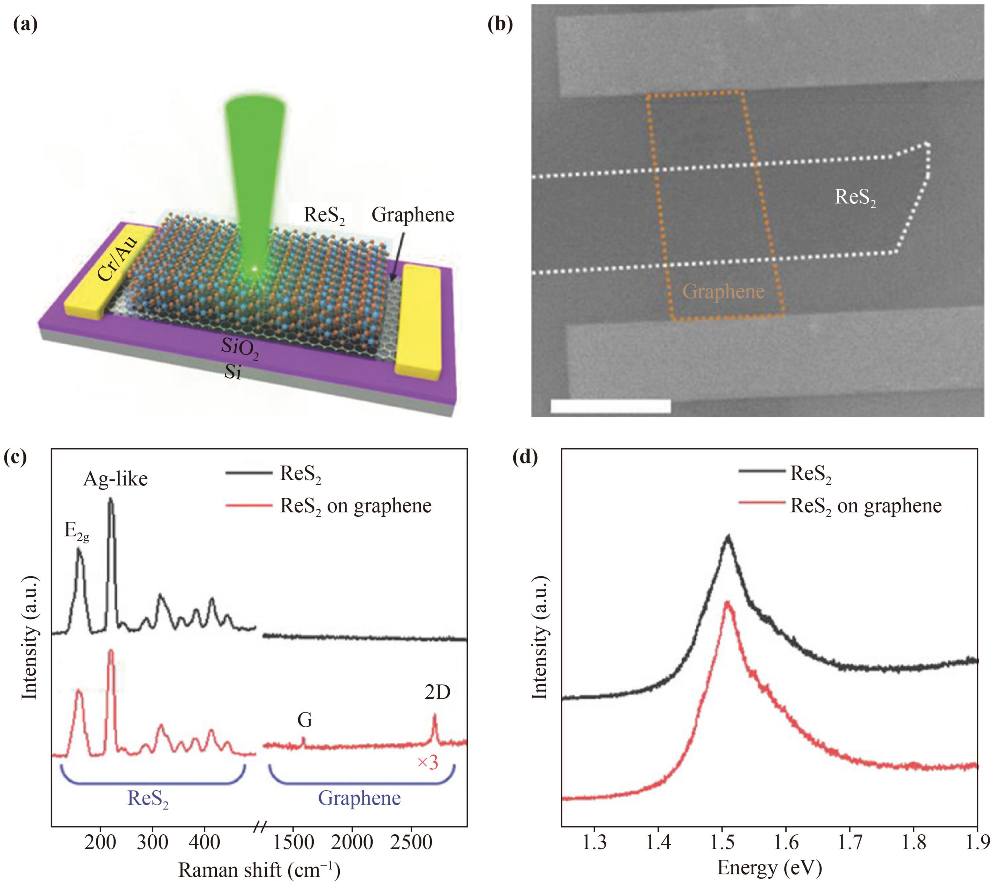

Fig. 10 **(a)** Schematic figure of ReS_2/graphene heterostructure optoelectronic device. **(b)** SEM image of the heterostructure. **(c)** Raman and **(d)** PL spectra of ReS_2 and heterostructure. Reproduced from Ref. [62].

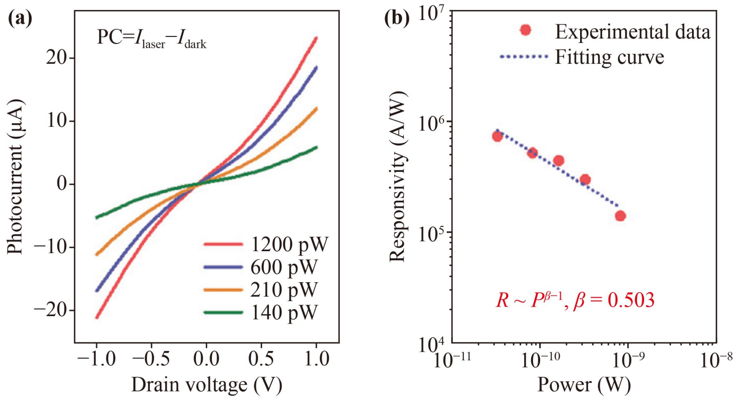

Fig. 11 **(a)** Photocurrent intensities of the heterojunction with different incident laser power. **(b)** Responsivity of heterojunction device and ReS$_2$ device. **(c)** The drain voltage dependent photocurrent of heterojunction device and ReS$_2$ device. Reproduced from Ref. [62].

the performance of heterojunction devices. The drain voltage dependent photocurrent reveals that the photocurrent of the hybrid device is 10^3 times than that generated by ReS$_2$, as shown in Fig. 11(c).

Kelvin probe force microscopy (KPFM) shows that the work functions of graphene and ReS$_2$ are similar. The electronic band structure is shown in Fig. 12(b). Since the close work function, the positions of the charge neutral point (CNP) are almost identical under dark and light conditions as shown in Fig. 12(c). The CNP displacement caused by the difference of work function ReS$_2$/graphene heterojunction is special in TMDCs/graphene heterojunction.

The ReS$_2$ photodetector shows a long response time because of low carrier mobility. For ReS$_2$/graphene heterojunction, when the photoexcited holes in the ReS$_2$ layer transfer to the graphene layer, the graphene immediately transfers carriers due to the high carrier mobility, which can improve response time as shown in Fig. 13(a). The heterojunction demonstrates fast rise time and decay time (30 ms). However, the rise and decay times of ReS$_2$ devices are both several seconds as shown in Fig. 13(c). When the temperature drops to 110 K, the responsivity increases slightly, and the photocurrent in Fig. 13(d) increases due to the decrease in the contact resistance of graphene and the graphene-metal.

4.4 The optoelectronic applications of perovskite/WS$_2$ heterostructures

Organic—inorganic hybrid perovskites shows outstanding optoelectrical properties, such as strong optical absorption ability, long carrier spread range, and adjustable band gap [66, 67], so it is widely used in photodetectors [37, 38], lasers [68], and LED [69, 70]. Chemical vapor deposition (CVD) method is used to obtain the monolayer WS$_2$ and 2D PbI$_2$ was deposited on WS$_2$ by vapor-phase selective deposition, and then converted into organic–inorganic Perovskite. 2D Perovskite/WS$_2$ heterostructures can be obtained by this method. Figures 14(a) and (b) show the STEM images of epitaxially ranged PbI$_2$/WS$_2$ heterostructure and the MAPbI$_3$/WS$_2$ heterostructure generated through inserting MAI. PL spectra of the heterojunction, WS$_2$ and perovskite show the quenching of PL peaks at 1.65 eV and 2 eV in the heterojunction, due to the charge transfer of electrons to WS$_2$ and holes to perovskite layers as shown in Fig. 14(d). And the heterojunction shows type II (staggered) energy band.

Figure 15(a) shows the optical micrograph taken from perovskite/WS$_2$ heterojunction with Au/Ni electrodes and the schematic, perovskite is formed between the source and drain. The $I-V$ characteristics of the heterostructure shows that when the laser wavelength is

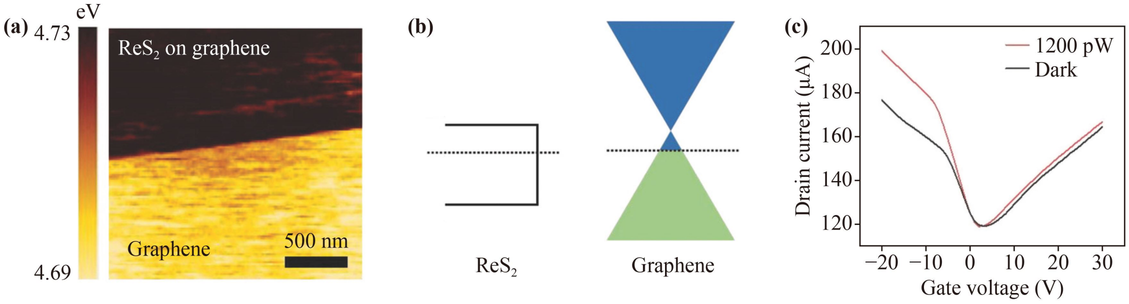

Fig. 12 **(a)** KPFM image taken from graphene and the ReS$_2$ on graphene. **(b)** The electronic band structure. **(c)** Transfer curves of the ReS$_2$/graphene heterostructure under dark and illumination. Reproduced from Ref. [62].

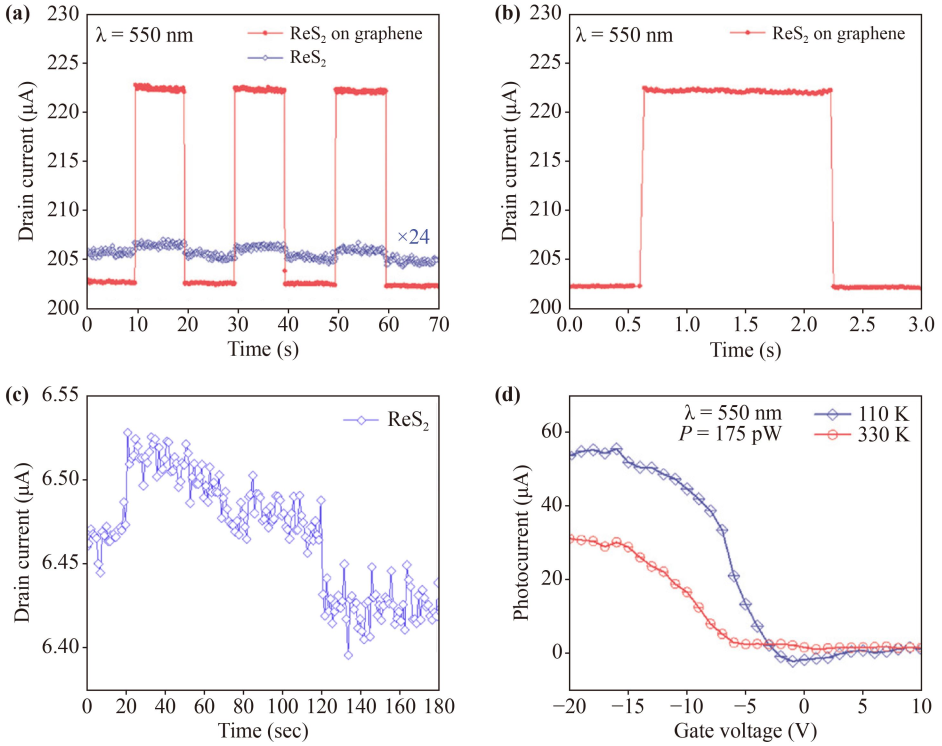

Fig. 13 **(a)** Photocurrent response time of ReS_2 and ReS_2/graphene heterostructure. **(b)** Photocurrent response time of ReS_2/graphene heterostructure with high time resolution. **(c)** Photocurrent response of the ReS_2 device. **(d)** Photocurrent taken from the heterojunction device at 110 or 330 K condition. Reproduced from Ref. [62].

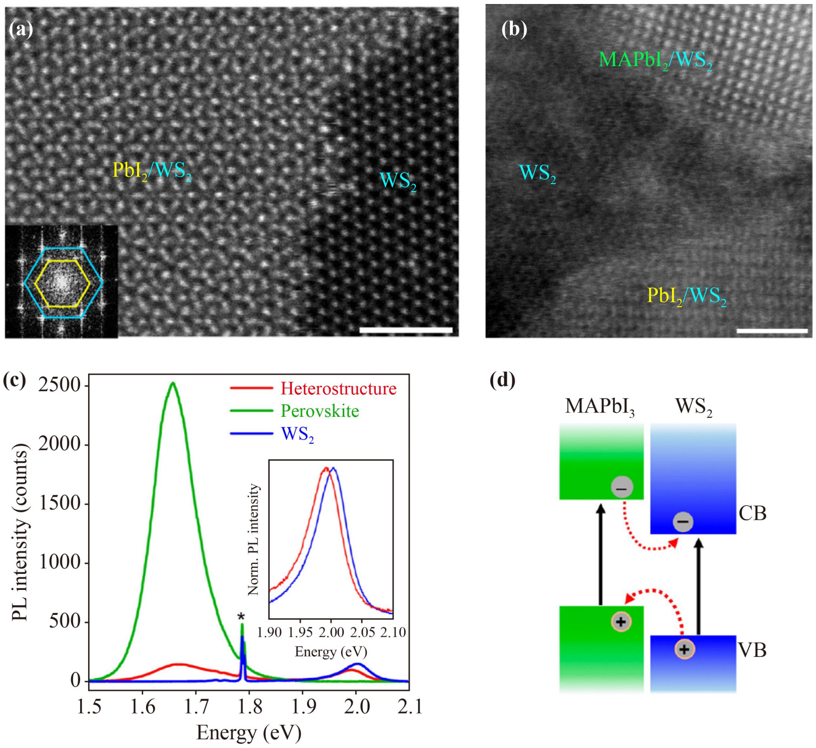

Fig. 14 **(a)** STEM image taken from PbI_2/WS_2 heterostructure. **(b)** STEM image taken from $MAPbI_3/WS_2$ heterostructure generated through inserting MAI. **(c)** PL spectra of heterostructure, separate perovskite and WS_2 layers. **(d)** Schematic of type II band alignment. Reproduced from Ref. [71].

532 nm and $V_g = 60$ V, high photocurrent generated by high laser power and the photocurrent value can reach 32.8 nA. When the optical power is 0.04 mW·cm^{-2}, the photoresponsivity is as high as 43.6 A·W^{-1}. As V_g increasing from 10 V to 20 V and 60 V, the photocurrent increases significantly with a 4.4 mW·cm^{-2} laser power and a V_d of 10 V, as shown in Fig. 15(c). Figure 15(d) demonstrates that perovskite/WS$_2$ heterojunction device demonstrates good stability and repeatability and is suitable for stable and reliable optoelectrical device.

4.5 Electrically driven graphene/h-BN/WSe$_2$ heterostructure-based emitter

The optoelectrical characteristics of TMDCs could be effectively controlled by strain [72–76], and TMDC-based emitters can be modulated by electricity. The energy band structures also change with the electric field [39, 77]. Graphene, several layers of h-BN, and WSe$_2$ were placed on the SiO$_2$/Si substrate in sequence. Finally, top graphene layer was placed on the WSe$_2$ to form the composite heterojunction as shown in Fig. 16(a). The strain is applied to the heterojunction material through atomic force microscope (AFM) tip. Tunneling effect can inject current into WSe$_2$ uniformly, which can be achieved by applying bias voltage to the graphene at top and bottom. When the bias is 0, no charge can pass through several layers of h-BN. However, when the bias is applied, the Fermi level rises to near conduction band of WSe$_2$, and electrons tunnel through the h-BN layers, which results in hole–electron radiative recombination [Fig. 16(b)]. Figures 16(c) and (d) show the optical microscope and AFM image of the heterostructure, respectively.

Obvious bright spots can be observed at 7 indentations from the EL spectrum with 2 V bias voltages [Fig. 17(a)], which is due to the strain that reduces the opening voltage of the tunneling current from 4 V to 1.5 V as shown in Fig. 17(b). The electroluminescence spectra at the seven indentation sites all have narrow single emission peaks from localized exciton states between 735 nm and 785 nm. The photon correlation functions $g^{(2)}(0)$ of 1–3 indentation sites are all less than the threshold line (0.5) and single-photon emission exhibit photon antibunching behavior. Substantially no background EL emission is observed, indicating the high purity of single-photon emission. The biased-dependent electroluminescence spectra showed a strong peak at 739.8 nm when the bias

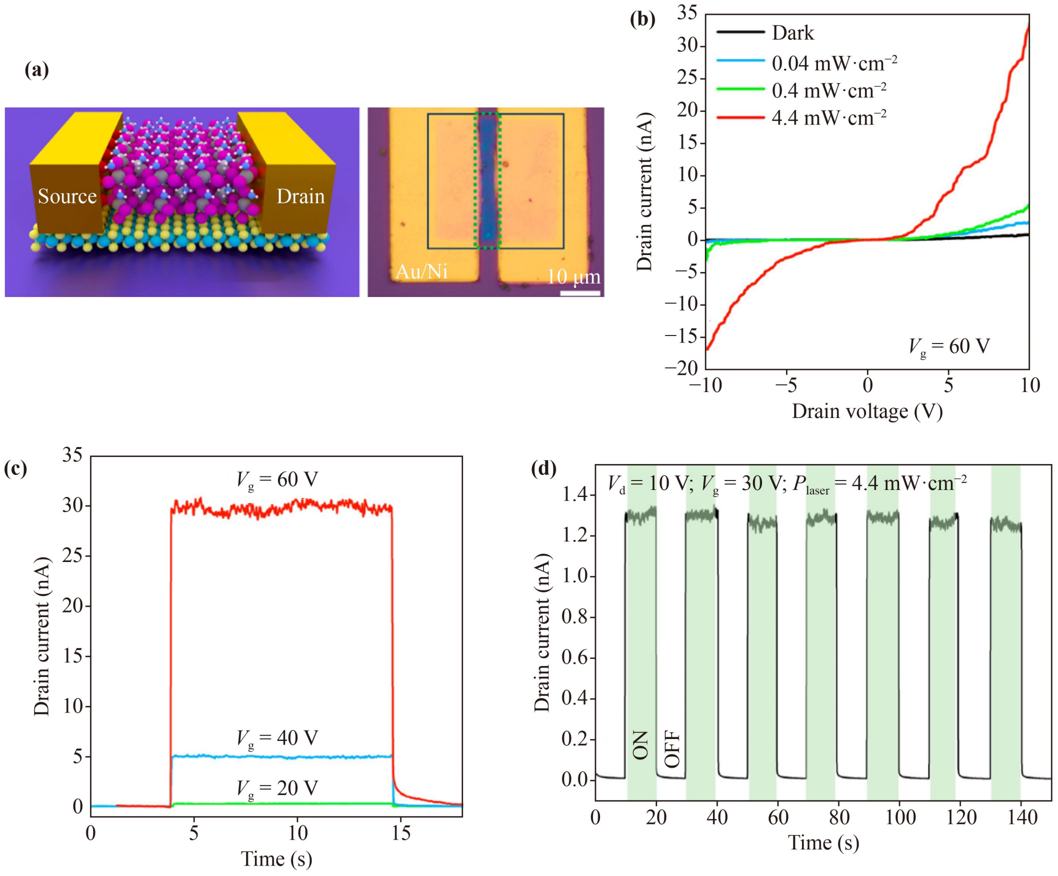

Fig. 15 **(a)** The schematic and the optical micrograph of the structure. **(b)** $I-V$ characteristics of the heterostructure photodetector in dark and different power laser conditions. **(c)** V_g-dependent photocurrent. **(d)** Time-resolved I_{drain} under dark and laser conditions. Reproduced from Ref. [71].

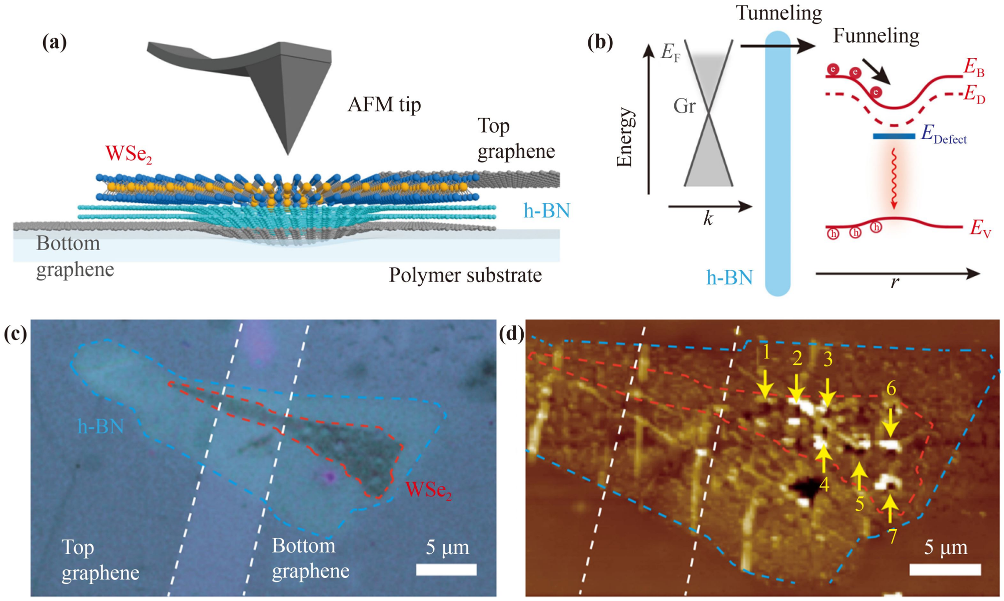

Fig. 16 **(a)** The model of graphene/WSe$_2$/h-BN/graphene heterostructure with an AFM tip. **(b)** The operating mechanism of the heterostructure device. **(c, d)** The optical microscope and AFM image taken from heterostructure, respectively. Reproduced from Ref. [78].

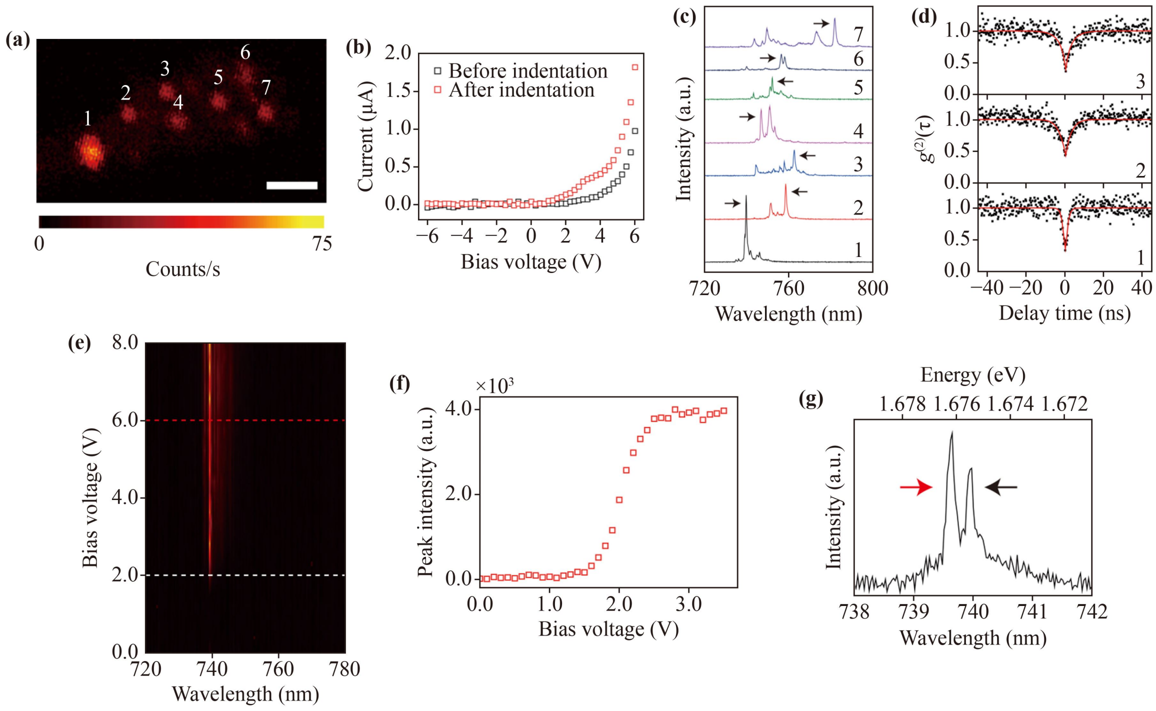

Fig. 17 **(a)** EL intensity map of the heterostructure. **(b)** The V_{Bais}-dependent Current before and after strain. **(c)** EL spectra of sites 1–7. **(d)** The second-order correlation function $g^{(2)}(\tau)$ of sites 1, 2, and 3. **(e)** V_{Bias}-dependent EL spectrum. **(f)** V_{Bais}-dependent EL peak intensity. **(g)** High-resolution EL spectrum. Reproduced from Ref. [78].

voltage was 1.5 V. As the bias increasing to 4 V, there are some small side peaks, which are consistent with Fig. 17(b), and the appearance of additional peaks leads to additional inflection points in the I–V curve. The peak strength increases rapidly from 1.5 V bias voltage and is saturated at 2.5 V bias voltage as shown in Fig. 17(f). The higher-resolution EL spectrum shows there is a fine structure splitting [Fig. 17(g)], which caused by the anisotropic electron–hole exchange interactions due to the strain-induced low symmetry.

5 Conclusion

As an important branch of layered nanomaterials, TMDCs materials not only show the excellent physical properties like graphene, but also make up the deficiency of graphene in photoelectric applications due to their zero bandgap and semi-metallic properties. First, TMDCs provide the basis for the formation of heterojunctions with excellent optoelectric properties due to their outstanding electronic band structure and operability. The rich interface structure provides convenient conditions for the construction of different types of heterojunctions. Second, the adjustable band gap of TMDCs material greatly expands its application in photoelectric sensor and other fields. TMDCs heterojunction materials have broad application prospects in photoelectric devices, flexible electronic devices, solar photovoltaic and photocatalysis. Through the design of the electronic band structure of the two materials that make up the heterojunction, the TMDCs heterojunctions can combine the advantages of the two or more materials to exhibit unique optoelectronic properties.

Acknowledgements This work was supported by the National Natural Science Foundation of China (Grant Nos. 91436102 and 11374353) and the Fundamental Research Funds for the Central Universities (Grant No. 06500067).

References

1. K. S. Novoselov, A. K. Geim, S. V. Morozov, D. E. Jiang, Y. Zhang, S. V. Dubonos, I. V. Grigorieva, and A. A. Firsov, Electric field effect in atomically thin carbon films, *Science* 306(5696), 666 (2004)
2. Y. Y. Li, B. Gao, Y. Han, B. K. Chen, and J. Y. Huo, Optoelectronic characteristics and application of black phosphorus and its analogs, *Front. Phys.* 16(4), 44301 (2021)
3. L. Li, Y. Yu, G. J. Ye, Q. Ge, X. Ou, H. Wu, D. Feng, X. H. Chen, and Y. Zhang, Black phosphorus field-effect transistors, *Nat. Nanotechnol.* 9(5), 372 (2014)
4. L. Britnell, R. M. Ribeiro, A. Eckmann, R. Jalil, B. D. Belle, A. Mishchenko, Y. J. Kim, R. V. Gorbachev, T. Georgiou, S. V. Morozov, A. N. Grigorenko, A. K. Geim, C. Casiraghi, A. H. C. Neto, and K. S. Novoselov, Strong light–matter interactions in heterostructures of atomically thin films, *Science* 340(6138), 1311 (2013)
5. Z. Q. Wang, T. Y. Lü, H. Q. Wang, Y. P. Feng, and J. C. Zheng, Review of borophene and its potential applications, *Front. Phys.* 14(3), 33403 (2019)
6. A. J. Mannix, X. F. Zhou, B. Kiraly, J. D. Wood, D. Alducin, B. D. Myers, X. Liu, B. L. Fisher, U. Santiago, J. R. Guest, M. J. Yacaman, A. Ponce, A. R. Oganov, M. C. Hersam, and N. P. Guisinger, Synthesis of borophenes: Anisotropic, two-dimensional boron polymorphs, *Science* 350(6267), 1513 (2015)
7. K. S. Novoselov, D. V. Andreeva, W. Ren, and G. Shan, Graphene and other two-dimensional materials, *Front. Phys.* 14(1), 13301 (2019)
8. G. H. Han, D. L. Duong, D. H. Keum, S. J. Yun, and Y. H. Lee, van der Waals metallic transition metal dichalcogenides, *Chem. Rev.* 118(13), 6297 (2018)
9. A. U. Liyanage and M. M. Lerner, Use of amine electride chemistry to prepare molybdenum disulfide intercalation compounds, *RSC Adv.* 4(87), 47121 (2014)
10. M. Chhowalla, H. S. Shin, G. Eda, L. J. Li, K. P. Loh, and H. Zhang, The chemistry of two-dimensional layered transition metal dichalcogenide nanosheets, *Nat. Chem.* 5(4), 263 (2013)
11. Q. Zhao, Y. Guo, Y. Zhou, X. Xu, Z. Ren, J. Bai, and X. Xu, Flexible and anisotropic properties of monolayer MX_2 (M = Tc and Re; X = S, Se), *J. Phys. Chem. C* 121(42), 23744 (2017)
12. M. Abdulsalam and D. P. Joubert, Optical spectrum and excitons in bulk and monolayer MX_2 (M = Zr, Hf; X = S, Se), *Phys. Status Solidi B* 253(4), 705 (2016) (b)
13. B. Radisavljevic, A. Radenovic, J. Brivio, V. Giacometti, and A. Kis, Single-layer MoS_2 transistors, *Nat. Nanotechnol.* 6(3), 147 (2011)
14. O. Lopez-Sanchez, D. Lembke, M. Kayci, A. Radenovic, and A. Kis, Ultrasensitive photodetectors based on monolayer MoS_2, *Nat. Nanotechnol.* 8(7), 497 (2013)
15. H. Zeng, J. Dai, W. Yao, D. Xiao, and X. Cui, Valley polarization in MoS_2 monolayers by optical pumping, *Nat. Nanotechnol.* 7(8), 490 (2012)
16. W. Zhang, C. P. Chuu, J. K. Huang, C. H. Chen, M. L. Tsai, Y. H. Chang, C. T. Liang, Y. Z. Chen, Y. L. Chueh, J. H. He, M. Y. Chou, and L. J. Li, Ultrahigh-gain photodetectors based on atomically thin graphene-MoS_2 heterostructures, *Sci. Rep.* 4(1), 3826 (2015)
17. C. Cong, J. Shang, X. Wu, B. Cao, N. Peimyoo, C. Qiu, L. Sun, and T. Yu, Synthesis and optical properties of large-area single-crystalline 2D semiconductor WS_2 monolayer from chemical vapor deposition, *Adv. Opt. Mater.* 2(2), 131 (2014)
18. T. LaMountain, E. J. Lenferink, Y. J. Chen, T. K. Stanev, and N. P. Stern, Environmental engineering of transition metal dichalcogenide optoelectronics, *Front. Phys.* 13(4), 138114 (2018)
19. Y. Liu, Y. Zhou, H. Zhang, F. Ran, W. Zhao, L. Wang, C. Pei, J. Zhang, X. Huang, and H. Li, Probing interlayer interactions in WSe_2-graphene heterostructures by ultralow-frequency Raman spectroscopy, *Front. Phys.* 14(1), 13607 (2019)
20. H. S. Lee, S. W. Min, Y. G. Chang, M. K. Park, T. Nam, H. Kim, J. H. Kim, S. Ryu, and S. Im, MoS_2 nanosheet phototransistors with thickness-modulated optical energy gap, *Nano Lett.* 12(7), 3695 (2012)
21. M. M. Furchi, A. Pospischil, F. Libisch, J. Burgdörfer, and T. Mueller, Photovoltaic effect in an electrically tunable van der Waals heterojunction, *Nano Lett.* 14(8), 4785 (2014)
22. G. Du, Z. Guo, S. Wang, R. Zeng, Z. Chen, and H. Liu, Superior stability and high capacity of restacked molybdenum disulfide as anode material for lithium ion batteries, *Chem. Commun.* 46(7), 1106 (2010)
23. M. Benameur, B. Radisavljevic, J. Héron, S. Sahoo, H. Berger, and A. Kis, Visibility of dichalcogenide nanolay-

ers, *Nanotechnology* 22(12), 125706 (2011)

24. Q. Ji, Y. Zhang, J. Shi, J. Sun, Y. Zhang, and Z. Liu, Morphological Engineering of CVD-grown transition metal dichalcogenides for efficient electrochemical hydrogen evolution, *Adv. Mater.* 28(29), 6207 (2016)
25. S. Imani Yengejeh, W. Wen, and Y. Wang, Mechanical properties of lateral transition metal dichalcogenide heterostructures, *Front. Phys.* 16(1), 13502 (2021)
26. X. Hong, J. Kim, S. F. Shi, Y. Zhang, C. Jin, Y. Sun, S. Tongay, J. Wu, Y. Zhang, and F. Wang, Ultrafast charge transfer in atomically thin MoS_2/WS_2 heterostructures, *Nat. Nanotechnol.* 9(9), 682 (2014)
27. M. L. Tsai, S. H. Su, J. K. Chang, D. S. Tsai, C. H. Chen, C. I. Wu, L. J. Li, L. J. Chen, and J. H. He, Monolayer MoS2 heterojunction solar cells, *ACS Nano* 8(8), 8317 (2014)
28. A. K. Geim and I. V. Grigorieva, Van der Waals heterostructures, *Nature* 499(7459), 419 (2013)
29. Y. Y. Wang, F. P. Li, W. Wei, B. B. Huang, and Y. Dai, Interlayer coupling effect in van der Waals heterostructures of transition metal dichalcogenides, *Front. Phys.* 16(1), 13501 (2021)
30. V. O. Özçelik, J. G. Azadani, C. Yang, S. J. Koester, and T. Low, Band alignment of two-dimensional semiconductors for designing heterostructures with momentum space matching, *Phys. Rev. B* 94(3), 035125 (2016)
31. Z. Zhou, S. Yuan, and J. Wang, Theoretical progress on direct Z-scheme photocatalysis of two-dimensional heterostructures, *Front. Phys.* 16(4), 43203 (2021)
32. D. Wijethunge, L. Zhang, C. Tang, and A. Du, Tuning band alignment and optical properties of 2D van der Waals heterostructure via ferroelectric polarization switching, *Front. Phys.* 15(6), 63504 (2020)
33. T. Wang, A. Dong, X. Zhang, R. K. Hocking, and C. Sun, Theoretical study of K_3Sb/graphene heterostructure for electrochemical nitrogen reduction reaction, *Front. Phys.* 17(2), 23501 (2022)
34. C. K. Kanade, H. Seok, V. K. Kanade, K. Aydin, H. U. Kim, S. B. Mitta, W. J. Yoo, and T. Kim, Low-temperature and large-scale production of a transition metal sulfide vertical heterostructure and its application for photodetectors, *ACS Appl. Mater. Interfaces* 13(7), 8710 (2021)
35. J. I. J. Wang, Y. Yang, Y. A. Chen, K. Watanabe, T. Taniguchi, H. O. Churchill, and P. Jarillo-Herrero, Electronic transport of encapsulated graphene and WSe_2 devices fabricated by pick-up of prepatterned hBN, *Nano Lett.* 15(3), 1898 (2015)
36. K. Chen, X. Wan, J. Wen, W. Xie, Z. Kang, X. Zeng, H. Chen, and J. B. Xu, Electronic properties of MoS_2–WS_2 heterostructures synthesized with two-step lateral epitaxial strategy, *ACS Nano* 9(10), 9868 (2015)
37. L. Dou, Y. M. Yang, J. You, Z. Hong, W. H. Chang, G. Li, and Y. Yang, Solution-processed hybrid perovskite photodetectors with high detectivity, *Nat. Commun.* 5(1), 5404 (2014)
38. Z. Yang, Y. Deng, X. Zhang, S. Wang, H. Chen, S. Yang, J. Khurgin, N. X. Fang, X. Zhang, and R. Ma, High-performance single-crystalline perovskite thin-film photodetector, *Adv. Mater.* 30(8), 1704333 (2018)
39. F. Withers, O. Del Pozo-Zamudio, A. Mishchenko, A. P. Rooney, A. Gholinia, K. Watanabe, T. Taniguchi, S. J. Haigh, A. K. Geim, A. I. Tartakovskii, and K. S. Novoselov, Light-emitting diodes by band-structure engineering in van der Waals heterostructures, *Nat. Mater.* 14(3), 301 (2015)
40. T. Georgiou, R. Jalil, B. D. Belle, L. Britnell, R. V. Gorbachev, S. V. Morozov, Y. J. Kim, A. Gholinia, S. J. Haigh, O. Makarovsky, L. Eaves, L. A. Ponomarenko, A. K. Geim, K. S. Novoselov, and A. Mishchenko, Vertical field-effect transistor based on graphene–WS_2 heterostructures for flexible and transparent electronics, *Nat. Nanotechnol.* 8(2), 100 (2013)
41. R. Cheng, D. Li, H. Zhou, C. Wang, A. Yin, S. Jiang, Y. Liu, Y. Chen, Y. Huang, and X. Duan, Electroluminescence and photocurrent generation from atomically sharp WSe_2/MoS_2 heterojunction p–n diodes, *Nano Lett.* 14(10), 5590 (2014)
42. D. Jariwala, V. K. Sangwan, L. J. Lauhon, T. J. Marks, and M. C. Hersam, Emerging device applications for semiconducting two-dimensional transition metal dichalcogenides, *ACS Nano* 8(2), 1102 (2014)
43. G. Eda, H. Yamaguchi, D. Voiry, T. Fujita, M. Chen, and M. Chhowalla, Photoluminescence from chemically exfoliated MoS_2, *Nano Lett.* 11(12), 5111 (2011)
44. Y. Ma, Y. Dai, M. Guo, C. Niu, and B. Huang, Graphene adhesion on MoS_2 monolayer: An *ab initio* study, *Nanoscale* 3(9), 3883 (2011)
45. Z. Huang, C. He, X. Qi, H. Yang, W. Liu, X. Wei, X. Peng, and J. Zhong, Band structure engineering of monolayer MoS_2 on h-BN: First-principles calculations, *J. Phys. D Appl. Phys.* 47(7), 075301 (2014)
46. Z. Huang, X. Qi, H. Yang, C. He, X. Wei, X. Peng, and J. Zhong, Band-gap engineering of the h-BN/MoS_2/h-BN sandwich heterostructure under an external electric field, *J. Phys. D Appl. Phys.* 48(20), 205302 (2015)
47. W. Yu, S. Li, Y. Zhang, W. Ma, T. Sun, J. Yuan, K. Fu, and Q. Bao, Near-infrared photodetectors based on $MoTe_2$/graphene heterostructure with high responsivity and flexibility, *Small* 13(24), 1700268 (2017)
48. X. Zhao, T. Huang, P. S. Ping, X. Wu, P. Huang, J. Pan, Y. Wu, and Z. Cheng, Sensitivity enhancement in surface plasmon resonance biochemical sensor based on transition metal dichalcogenides/graphene heterostructure, *Sensors (Basel)* 18(7), 2056 (2018)
49. Q. Lv and R. Lv, Two-dimensional heterostructures based on graphene and transition metal dichalcogenides: synthesis, transfer and applications, *Carbon* 145, 240 (2019)
50. S. Nakamura, M. Senoh, N. Iwasa, and S. N. S. i. Nagahama, High-brightness InGaN blue, green and yellow light-emitting diodes with quantum well structures, *Jpn. J. Appl. Phys.* 34, L797 (1995)
51. Q. A. Vu and W. J. Yu, Electronics and optoelectronics based on two-dimensional materials, *J. Korean Phys. Soc.* 73(1), 1 (2018)
52. S. O. Koswatta, S. J. Koester, and W. Haensch, On the possibility of obtaining MOSFET-like performance and sub-60-mV/dec swing in 1-D broken-gap tunnel transistors, *IEEE Trans. Electron Dev.* 57(12), 3222 (2010)
53. Y. Zhang, W. Ma, Y. Cao, J. Huang, Y. Wei, K. Cui, and J. Shao, Long wavelength infrared InAs/GaSb superlattice photodetectors with InSb-like and mixed

interfaces, *IEEE J. Quantum Electron.* 47(12), 1475 (2011)

54. Q. Zhao, Y. Guo, K. Si, Z. Ren, J. Bai, and X. Xu, Elastic, electronic, and dielectric properties of bulk and monolayer ZrS_2, $ZrSe_2$, HfS_2, $HfSe_2$ from van der Waals density-functional theory, *physica status solidi (b)* 254, 1700033 (2017)
55. Q. Zhao, Y. Guo, Y. Zhou, Z. Yao, Z. Ren, J. Bai, and X. Xu, Band alignments and heterostructures of monolayer transition metal trichalcogenides MX_3 (M= Zr, Hf; X= S, Se) and dichalcogenides MX_2 (M= Tc, Re; X= S, Se) for solar applications, *Nanoscale* 10(7), 3547 (2018)
56. X. Mu and M. Sun, Interfacial charge transfer exciton enhanced by plasmon in 2D in-plane lateral and van der Waals heterostructures, *Appl. Phys. Lett.* 117(9), 091601 (2020)
57. J. Fan, J. Song, Y. Cheng, and M. Sun, Pressure-dependent interfacial charge transfer excitons in WSe_2-MoSe_2 heterostructures in near infrared region, *Results Phys.* 24, 104110 (2021)
58. X. H. Li, Y. X. Guo, Y. Ren, J. J. Peng, J. S. Liu, C. Wang, and H. Zhang, Narrow-bandgap materials for optoelectronics applications, *Front. Phys.* 17(1), 13304 (2022)
59. Z. Z. Yan, Z. H. Jiang, J. P. Lu, and Z. H. Ni, Interfacial charge transfer in WS_2 monolayer/$CsPbBr_3$ microplate heterostructure, *Front. Phys.* 13(4), 138115 (2018)
60. N. Zhang, J. Wu, T. Yu, J. Lv, H. Liu, and X. Xu, Theory, preparation, properties and catalysis application in 2D graphynes-based materials, *Front. Phys.* 16(2), 23201 (2021)
61. C. Lan, C. Li, S. Wang, T. He, Z. Zhou, D. Wei, H. Guo, H. Yang, and Y. Liu, Highly responsive and broadband photodetectors based on WS_2–graphene van der Waals epitaxial heterostructures, *J. Mater. Chem. C* 5(6), 1494 (2017)
62. B. Kang, Y. Kim, W. J. Yoo, and C. Lee, Ultrahigh photoresponsive device based on ReS_2/graphene heterostructure, *Small* 14(45), 1802593 (2018)
63. H. Xu, J. Wu, Q. Feng, N. Mao, C. Wang, and J. Zhang, High responsivity and gate tunable grapheme-MoS_2 hybrid phototransistor, *Small* 10(11), 2300 (2014)
64. X. Song, X. Liu, D. Yu, C. Huo, J. Ji, X. Li, S. Zhang, Y. Zou, G. Zhu, Y. Wang, M. Wu, A. Xie, and H. Zeng, Boosting two-dimensional MoS_2/$CsPbBr_3$ photodetectors via enhanced light absorbance and interfacial carrier separation, *ACS Appl. Mater. Interfaces* 10(3), 2801 (2018)
65. C. Huo, X. Liu, Z. Wang, X. Song, and H. Zeng, High-performance low-voltage-driven phototransistors through $CsPbBr_3$–2D crystal van der Waals heterojunctions, *Adv. Opt. Mater.* 6(16), 1800152 (2018)
66. S. D. Stranks and H. J. Snaith, Metal-halide perovskites for photovoltaic and light-emitting devices, *Nat. Nanotechnol.* 10(5), 391 (2015)
67. H. S. Jung and N. G. Park, Perovskite solar cells: From materials to devices, *Small* 11(1), 10 (2015)
68. G. Xing, N. Mathews, S. S. Lim, N. Yantara, X. Liu, D. Sabba, M. Grätzel, S. Mhaisalkar, and T. C. Sum, Low-temperature solution-processed wavelength-tunable perovskites for lasing, *Nat. Mater.* 13(5), 476 (2014)
69. H. Kim, L. Zhao, J. S. Price, A. J. Grede, K. Roh, A. N. Brigeman, M. Lopez, B. P. Rand, and N. C. Giebink, Hybrid perovskite light emitting diodes under intense electrical excitation, *Nat. Commun.* 9(1), 4893 (2018)
70. S. Kumar, J. Jagielski, N. Kallikounis, Y. H. Kim, C. Wolf, F. Jenny, T. Tian, C. J. Hofer, Y. C. Chiu, W. J. Stark, T. W. Lee, and C. J. Shih, Ultrapure green light-emitting diodes using two-dimensional formamidinium perovskites: Achieving recommendation 2020 color coordinates, *Nano Lett.* 17(9), 5277 (2017)
71. U. Erkılıç, P. Solís-Fernández, H. G. Ji, K. Shinokita, Y. C. Lin, M. Maruyama, K. Suenaga, S. Okada, K. Matsuda, and H. Ago, Vapor phase selective growth of two-dimensional perovskite/WS_2 heterostructures for optoelectronic applications, *ACS Appl. Mater. Interfaces* 11(43), 40503 (2019)
72. C. Palacios-Berraquero, D. M. Kara, A. R. P. Montblanch, M. Barbone, P. Latawiec, D. Yoon, A. K. Ott, M. Loncar, A. C. Ferrari, and M. Atatüre, Large-scale quantum-emitter arrays in atomically thin semiconductors, *Nat. Commun.* 8(1), 15093 (2017)
73. G. D. Shepard, O. Ajayi, X. Li, X.-Y. Zhu, J. Hone, and S. Strauf, Nanobubble induced formation of quantum emitters in monolayer semiconductors, *2D Mater.* 4, 021019 (2017)
74. F. Peyskens, C. Chakraborty, M. Muneeb, D. Van Thourhout, and D. Englund, Integration of single photon emitters in 2D layered materials with a silicon nitride photonic chip, *Nat. Commun.* 10(1), 4435 (2019)
75. M. Blauth, M. Jürgensen, G. Vest, O. Hartwig, M. Prechtl, J. Cerne, J. J. Finley, and M. Kaniber, Coupling single photons from discrete quantum emitters in WSe_2 to lithographically defined plasmonic slot waveguides, *Nano Lett.* 18(11), 6812 (2018)
76. Y. Luo, G. D. Shepard, J. V. Ardelean, D. A. Rhodes, B. Kim, K. Barmak, J. C. Hone, and S. Strauf, Deterministic coupling of site-controlled quantum emitters in monolayer WSe_2 to plasmonic nanocavities, *Nat. Nanotechnol.* 13(12), 1137 (2018)
77. F. Withers, O. Del Pozo-Zamudio, S. Schwarz, S. Dufferwiel, P. Walker, T. Godde, A. Rooney, A. Gholinia, C. Woods, P. Blake, S. J. Haigh, K. Watanabe, T. Taniguchi, I. L. Aleiner, A. K. Geim, V. I. Fal' ko, A. I. Tartakovskii, and K. S. Novoselov, WSe_2 light-emitting tunneling transistors with enhanced brightness at room temperature, *Nano Lett.* 15(12), 8223 (2015)
78. J. P. So, H. R. Kim, H. Baek, K. Y. Jeong, H. C. Lee, W. Huh, Y. S. Kim, K. Watanabe, T. Taniguchi, J. Kim, C. H. Lee, and H. G. Park, Electrically driven strain-induced deterministic single-photon emitters in a van der Waals heterostructure, *Sci. Adv.* 7(43), eabj3176 (2021)